Run-Up of Solitary Waves on Twin Conical Islands Using a Boussinesq Model

Run-up of Solitary Waves on Twin Conical Islands Using a Boussinesq Model

Dr Dongfang Liang

Department of Engineering, University of Cambridge,

Trumpington Street, Cambridge CB2 1PZ, UK

Tel: +44 1223 764829; Fax: +44 1223 332662; E-mail: d.liang@eng.cam.ac.uk

Professor Alistair G. L. Borthwick

Department of Engineering Science, University of Oxford,

Parks Road, Oxford OX1 3PJ, UK

Tel: +44 1865 273047; Fax: +44 1865 273010; E-mail: alistair.borthwick@eng.ox.ac.uk

Mr Jonathan K. Romer-Lee

Department of Engineering, University of Cambridge,

Trumpington Street, Cambridge CB2 1PZ, UK

E-Mail: jr415@cam.ac.uk

Abstract

This paper investigates the interaction of solitary waves (representative of tsunamis) with idealised flat-topped conical islands. The investigation is based on simulations produced by a numerical model that solves the two-dimensional Boussinesq-type equations of Madsen and Sørensen using a Total Variation Diminishing (TVD) Lax-Wendroff scheme. After verification against published laboratory data on solitary wave run-up at a single island, the numerical model is applied to study the maximum run-up at a pair of identical conical islands located at different spacing apart for various angles

of wave attack. The predicted results indicate that the maximum run-up can be attenuated or enhancement according to the position of the second island, because of wave refraction, diffraction and reflection. It is also observed that the local wave height and hence run-up can be amplified at certain gap spacing between the islands, owing to the interference between the incident waves and the reflected waves between islands.

Keywords: Solitary wave; tsunami; shock-capturing; TVD; Boussinesq equations.

1. Introduction

Tsunamis are extreme events that can wreak havoc in vulnerable coastal regions, such as low-lying settlements on islands in the Pacific Ocean. For example, Babi Island - a small conical island 5 km northwest of Flores Island, Indonesia - was badly hit by a tsunami on December 12th 1992, leaving a quarter of the population dead. In particular, two villages situated on the lee side of the island during the tsunami strike were both completely destroyed (Tsuji *et al.* 1995). As Briggs *et al.* (2005) note "this is an interesting phenomenon, since most people would feel 'safe' on the backside of an island". Various researchers including Liu *et al.* (1995) and Briggs *et al.* (1995) conducted experiments on solitary wave interaction with a single flat-topped conical island (an idealisation of a typical volcanic island). Liu *et al.* suggest that wave refraction and diffraction were most likely to be responsible for the enhancement of run-up that exacerbated the destruction witnessed to the lee side villages in Babi Island, Indonesia as well as Okushiri Island, Japan. In their comprehensive report on the Indian Ocean tsunami of December 26, 2004, Lavigne *et al.* (2009) note that wave reflection could also have been a further contributory factor to the local amplification of the

tsunami effects at Babi Island (see Yeh *et al.* 1994, Minoura *et al.* 1997). Gently sloping circular islands (e.g. Veti Levu - the principal island of Fiji) are common in regions highly susceptible to tsunamis from tectonic activity, such as the Eastern Indian Ocean or the Pacific Rim. Numerical simulations of tsunami-like waves have been made using the shallow-water approximations (e.g. Liu *et al.* 1995, Titov and Synolakis 1998, Wei *et al.* 2006) and Boussinesq models (e.g. Chen *et al.* 2000, Fuhrman and Madsen 2008).

Clusters of islands are prevalent in the Caribbean and Pacific Rim (Jacaranda 2002). In island clusters, the disturbance to the wave field induced by the presence of neighbouring islands can have a significant influence on the wave run-up on a given island. With this scenario in mind, the present paper aims to investigate an idealised form of tsunami run-up on a very simple island cluster: namely, solitary wave run-up at a pair of adjacent islands. To achieve this, a robust numerical model that solves the Boussinesq equations was developed using the TVD Lax-Wendroff scheme. The model was first applied to simulate solitary wave run-up at a single conical island, and the results compared with laboratory measurements reported by Briggs *et al.* (1995) and Liu *et al.* (1995). The predicted and measured results are found to be in satisfactory agreement, thus validating the numerical model. Then, an additional nearby island was added to the single island configuration, and the changes of wave run-up behaviour were examined. The nearby island is found to either provide sheltering to its neighbour, or else amplify the run-up. The computational results are sensible in terms of solitary wave diffraction and reflection. The numerical model developed in the present study could be applied as a tool to help predict the severity of tsunami risk at different island locations, with a view of making appropriate crisis response preparations.

2. TVD Lax-Wendroff scheme for Boussinesq model

2.1. Mathematical model

The shallow water Boussinesq-type equations due to Madsen and Sørensen (1992) can be written in the following matrix-vector form (see e.g. Borthwick *et al.* 2005, Ning *et al.* 2008):

$$\mathbf{X}_t + \mathbf{F}_x + \mathbf{G}_y = \mathbf{S} + \mathbf{T} \tag{1}$$

where the subscripts t, x and y denote the differentiation with respect to time and two spatial coordinates, and the vectors are:

$$\mathbf{X} = \begin{bmatrix} \eta \\ p \\ q \end{bmatrix},\ \mathbf{F} = \begin{bmatrix} p \\ \dfrac{p^2}{d} + \dfrac{g\eta^2}{2} + gh\eta \\ \dfrac{pq}{d} \end{bmatrix},\ \mathbf{G} = \begin{bmatrix} q \\ \dfrac{pq}{d} \\ \dfrac{q^2}{d} + \dfrac{g\eta^2}{2} + gh\eta \end{bmatrix}, \tag{2a, b, c}$$

$$\mathbf{S} = \begin{bmatrix} 0 \\ g\eta h_x - \dfrac{n^2 gp\sqrt{p^2+q^2}}{d^{7/3}} + \varphi \\ 0 \end{bmatrix},\ \mathbf{T} = \begin{bmatrix} 0 \\ 0 \\ g\eta h_y - \dfrac{n^2 gq\sqrt{p^2+q^2}}{d^{7/3}} + \psi \end{bmatrix}, \tag{2d, e}$$

in which η is the free-surface displacement above the still water level, $d = \eta + h$ is the total water depth with h being the still water depth, p and q are the horizontal components of the volume flux in the x and y directions respectively, g is the acceleration due to gravity (=9.81 m/s^2), n is the Manning roughness coefficient, and φ and ψ are the Boussinesq dispersive terms defined as:

$$\varphi = (B+\frac{1}{3})h^2(p_{xxt}+q_{xyt}) + Bgh^3(\eta_{xxx}+\eta_{xyy}) + hh_x(\frac{1}{3}p_{xt}+\frac{1}{6}q_{yt}+2Bgh\eta_{xx}+Bgh\eta_{yy}) + hh_y(\frac{1}{6}q_{xt}+Bgh\eta_{xy}) \quad , \quad (3a)$$

and

$$\psi = (B+\frac{1}{3})h^2(q_{yyt}+p_{xyt}) + Bgh^3(\eta_{yyy}+\eta_{xxy}) + hh_y(\frac{1}{3}q_{yt}+\frac{1}{6}p_{xt}+2Bgh\eta_{yy}+Bgh\eta_{xx}) + hh_x(\frac{1}{6}p_{yt}+Bgh\eta_{xy}) \quad , \quad (3b)$$

for which B (= 1/15) is the dispersion coefficient. By subtracting these dispersive terms from Equations (2d,e), Equation (1) reduces into the non-linear shallow water equations.

2.2. Overall solution strategy

With the operator-splitting technique, the solution of Equation (1) can be approached by solving the following two one-dimensional problems alternately:

$$\mathbf{X}_t + \mathbf{F}_x = \mathbf{S} \quad \text{and} \quad \mathbf{X}_t + \mathbf{G}_y = \mathbf{T} . \quad (4a,b)$$

The present computation is carried out on a uniform Cartesian grid. The finite difference scheme for Equations (4a,b) can be expressed as:

$$\mathbf{X}_{i,j}^{n+1} = \mathrm{L}_x \mathbf{X}_{i,j}^{n} \quad \text{and} \quad \mathbf{X}_{i,j}^{n+1} = \mathrm{L}_y \mathbf{X}_{i,j}^{n} \quad , \quad (5a, b)$$

where L_x and L_y are the finite-difference operators, and the subscript and superscript of **X** denote the spatial and temporal indices respectively. Following Strang (1968), the finite difference scheme for Equation (1) can be constructed as:

$$\mathbf{X}_{i,j}^{n+2} = \mathrm{L}_x\mathrm{L}_y\mathrm{L}_y\mathrm{L}_x \mathbf{X}_{i,j}^{n} \quad . \quad (6)$$

It is seen from Equation (3) that φ and ψ include many mixed second-order and third-order derivatives, which greatly complicate the solution procedure. Following Bradford

and Sanders (2002) and Borthwick *et al.* (2006), both Equation (4a) and Equation (4b) are solved in two steps. First, the following hyperbolic equations are solved:

$$\mathbf{U}_t + \mathbf{F}_x = \mathbf{S}^* \quad \text{and} \quad \mathbf{V}_t + \mathbf{G}_y = \mathbf{T}^* \tag{7a,b}$$

where

$$\mathbf{U} = \begin{bmatrix} \eta \\ p^* \\ q \end{bmatrix} = \begin{bmatrix} \eta \\ p - (B + \frac{1}{3})h^2(p_{xx} + q_{xy}) - hh_x(\frac{1}{3}p_x + \frac{1}{6}q_y) - \frac{1}{6}hh_y q_x \\ q \end{bmatrix}, \tag{8a}$$

$$\mathbf{V} = \begin{bmatrix} \eta \\ p \\ q^* \end{bmatrix} = \begin{bmatrix} \eta \\ p \\ q - (B + \frac{1}{3})h^2(q_{yy} + p_{xy}) - hh_y(\frac{1}{3}q_y + \frac{1}{6}p_x) - \frac{1}{6}hh_x p_y \end{bmatrix}, \tag{8b}$$

$$\mathbf{S}^* = \begin{bmatrix} 0 \\ g\eta h_x - \dfrac{n^2 gp\sqrt{p^2+q^2}}{d^{7/3}} + Bgh^3(\eta_{xxx} + \eta_{xyy}) + Bgh^2 h_x(2\eta_{xx} + \eta_{yy}) + Bgh^2 h_y \eta_{xy} \\ 0 \end{bmatrix}, \tag{8c}$$

and

$$\mathbf{T}^* = \begin{bmatrix} 0 \\ 0 \\ g\eta h_y - \dfrac{n^2 gq\sqrt{p^2+q^2}}{d^{7/3}} + Bgh^3(\eta_{yyy} + \eta_{xxy}) + Bgh^2 h_y(2\eta_{yy} + \eta_{xx}) + Bgh^2 h_x \eta_{xy} \end{bmatrix}. \tag{8d}$$

Equations 8(a-b) reveal that p^*, q^* and p, q are related by elliptic equations. Therefore, the primary variables, [η, p, q], can be determined easily after **U** and **V** are obtained. Taking Equation 8(a) for example, the central difference expression for p^* is:

$$p^*_{i,j} = p_{i,j} - \left(B + \frac{1}{3}\right) \cdot h_{i,j}^{\,2} \cdot \left(\frac{p_{i+1,j} - 2p_{i,j} + p_{i-1,j}}{\Delta x^2} + \frac{q_{i+1,j+1} - q_{i-1,j} - q_{i,j-1} + q_{i+1,j+1}}{4\Delta x^2} \right)$$
$$- h_{i,j} \cdot \frac{h_{i+1,j} - h_{i-1,j}}{2\Delta x} \cdot \left(\frac{1}{3} \cdot \frac{p_{i+1,j} - p_{i-1,j}}{2\Delta x} + \frac{1}{6} \cdot \frac{q_{i,j+1} - q_{i,j-1}}{2\Delta x} \right) \qquad (9)$$
$$- \frac{1}{6} \cdot h_{i,j} \cdot \frac{h_{i,j+1} - h_{i,j-1}}{2\Delta x} \cdot \frac{q_{i+1,j} - q_{i-1,j}}{2\Delta x}$$

where Δx is the grid size. Knowing p^* and q across the domain, Equation (9) forms a linear system of equations, from which p can be solved. Likewise, q can be obtained according to Equation (8b) once p and q^* are known.

An illustration of the solution procedure is given in Figure 1.

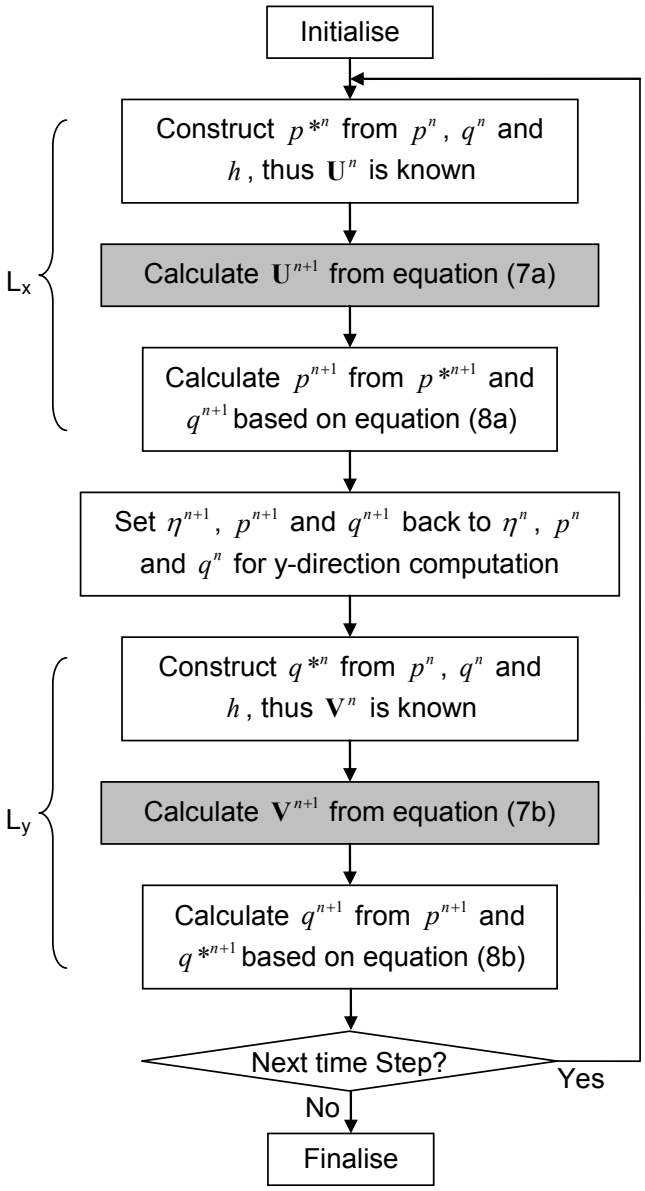

Fig. 1. Computational procedure

It should be noted that sequence of executing operators L_x and L_y is alternated in the actual computation as indicated in Equation (6), although this is not reflected in Figure 1. Ning *et al.* (2008) reported a similar algorithm. The advantage of the present approach lies in the efficient calculation of p^{n+1} and q^{n+1} from p^{*n+1} and q^{*n+1} using the tri-diagonal matrix algorithm, which is enabled by the operator-splitting technique.

2.3 TVD Lax-Wendroff scheme

The TVD Lax-Wendroff scheme is used to march from $\mathbf{U}^n$ to $\mathbf{U}^{n+1}$ and from $\mathbf{V}^n$ to $\mathbf{V}^{n+1}$ according to Equation (7a) and Equation (7b) respectively (and indicated by the grey boxes in Figure 1). Since the two one-dimensional problems are similar, it suffices to consider only Equation (7a) along a single row i, with the subscript j being dropped for clarity.

A symmetric non-linear flux limiter is appended to the conventional two-step Lax-Wendroff scheme, giving second-order accuracy in both time and space. Such a scheme is a member of the conventional shock-capturing finite difference schemes proposed in aerodynamics (Davis 1984). The flux limiter is designed to satisfy the TVD criterion, and has been adopted in developing the TVD-MacCormack model for shallow water flows (see e.g. Liang *et al*. 2007).

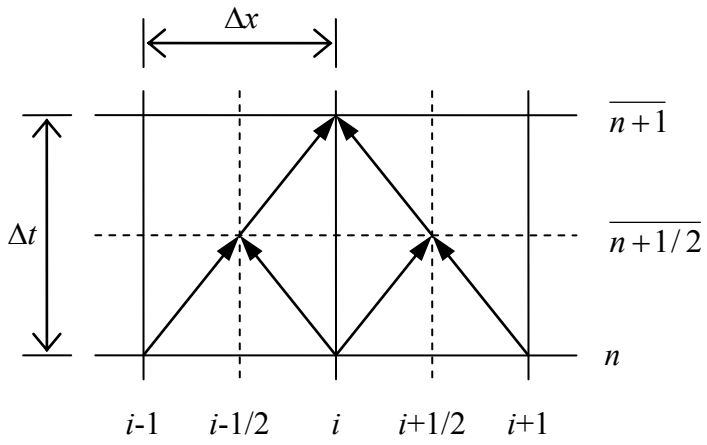

Fig. 2. Computational stencil for two-step Lax-Wendroff scheme

The standard two-step Lax-Wendroff scheme is based on the computational stencil shown in Figure 2. The first step calculates the values at half time steps and half grid points using space-centred and time-forward differencing, whilst the second step uses centred differencing in both time and space, such that

$$\mathbf{U}_{i+1/2}^{\overline{n+1/2}} = \frac{1}{2}\left(\mathbf{U}_{i+1}^{n} + \mathbf{U}_{i}^{n}\right) - \frac{\Delta t}{2\Delta x}\left(\mathbf{F}_{i+1}^{n} - \mathbf{F}_{i}^{n}\right) + \frac{\Delta t}{4}\left(\mathbf{S}*_{i+1}^{n} + \mathbf{S}*_{i}^{n}\right) \qquad (10\text{~~9~~}a)$$

and

$$\mathbf{U}_{i}^{\overline{n+1}} = \mathbf{U}_{i}^{n} - \frac{\Delta t}{\Delta x}\left(\mathbf{F}_{i+1/2}^{\overline{n+1/2}} - \mathbf{F}_{i-1/2}^{\overline{n+1/2}}\right) + \frac{\Delta t}{2}\left(\mathbf{S}*_{i+1/2}^{\overline{n+1/2}} + \mathbf{S}*_{i-1/2}^{\overline{n+1/2}}\right) \quad . \qquad (\text{~~9~~}10b)$$

Δx and Δt are the grid size and time step respectively. The overbars in Figure 2 and Equations (~~9a~~10a,b) signify that a full time step is achieved only after the following TVD modification is implemented:

$$\mathbf{U}_{i}^{n+1} = \mathbf{U}_{i}^{\overline{n+1}} + \left[\mathrm{G}(r_{i}^{+}) + \mathrm{G}(r_{i+1}^{-})\right]\cdot\Delta\mathbf{U}_{i+1/2}^{n} - \left[\mathrm{G}(r_{i-1}^{+}) + \mathrm{G}(r_{i}^{-})\right]\cdot\Delta\mathbf{U}_{i-1/2}^{n} \qquad (\text{~~10~~}11)$$

where

$$\Delta\mathbf{U}_{i+1/2}^{n} = \mathbf{U}_{i+1}^{n} - \mathbf{U}_{i}^{n} \quad , \qquad (1\text{~~1~~}2)$$

$$r_{i}^{+} = \frac{\left\langle \Delta\mathbf{U}_{i-1/2}^{n}, \Delta\mathbf{U}_{i+1/2}^{n} \right\rangle}{\left\langle \Delta\mathbf{U}_{i+1/2}^{n}, \Delta\mathbf{U}_{i+1/2}^{n} \right\rangle}, \quad r_{i}^{-} = \frac{\left\langle \Delta\mathbf{U}_{i-1/2}^{n}, \Delta\mathbf{U}_{i+1/2}^{n} \right\rangle}{\left\langle \Delta\mathbf{U}_{i-1/2}^{n}, \Delta\mathbf{U}_{i-1/2}^{n} \right\rangle} \quad , \qquad (1\text{~~2~~}3a,\ b)$$

and

$$\mathrm{G}(r_{i}) = 0.5 \times C_{i} \times \left[1 - \phi(r_{i})\right] \quad . \qquad (1\text{~~3~~}4)$$

The angle bracket in Equations (1~~2~~3a, b) denotes the dot product of the two vectors within the bracket. C_i is dependent on the local Courant number Cr_i, such that

$$C_{i} = \begin{cases} Cr_{i} \times (1 - Cr_{i}), & \text{if } Cr_{i} \le 0.5 \\ 0.25, & \text{else} \end{cases} \qquad (1\text{~~2~~}5)$$

with

$$Cr_{i} = \frac{\left(\left|p_{i}/d_{i}\right| + \sqrt{gd_{i}}\right)\Delta t}{\Delta x} \quad . \qquad (1\text{~~3~~}6)$$

$\phi(r_i)$ is a non-linear flux limiter defined as

$$\phi(r_{i}) = \max\left(0, \min(2r_{i}, 1)\right) \quad . \qquad (1\text{~~4~~}7)$$

The standard Lax-Wendroff scheme is second-order accurate. The Godunov theorem (Godunov 1959) states that all second-order schemes having constant coefficients will generate spurious oscillations at discontinuities. The non-linear TVD step essentially evaluates the smoothness of the solution using the ratios of the successive increments, as shown in Equations (11-12-123). Where the solution varies steeply and the local Courant number is large, sufficient diffusion is introduced to avoid spurious oscillations. On the contrary, little diffusion is introduced where the solution is smooth or the Courant number is small. Unlike most other TVD schemes, no characteristic transformation is needed in the present method.

Liang (2010b) has applied this TVD Lax-Wendroff scheme to solve the shallow water equations. A noteworthy property of this scheme is that the discharge of the flow is exactly balanced if the variable, $\mathbf{F}_{i+1/2}^{n+1/2}$, is treated as the flux output, no matter whether the fluid is in stationary, steady flow or unsteady flow state. Hence,

$$\mathbf{F}_{i+1/2}^{n+1/2} = \overline{\mathbf{F}_{i+1/2}^{n+1/2}} - \left[\mathrm{G}(r_i^+) + \mathrm{G}(r_{i+1}^-)\right] \cdot \Delta\mathbf{U}_{i+1/2}^{n} \cdot \frac{\Delta x}{\Delta t} \qquad (15\text{-}8)$$

Further details can be found in Liang (2010b).

3. Computational conditions

The high quality large-scale experimental results obtained by Liu *et al.* (1995) and Briggs *et al.* (1995) are widely used as benchmark data for validating numerical models of solitary wave interaction with an island (see e.g. Titov and Synolakis 1998, Chen *et al.* 2000, Wei *et al.* 2006, Fuhrman and Madsen 2008). Here, we consider a test case taken from Liu *et al.* (1995) whose laboratory basin was rectangular in plan, of dimensions 30m wide (x direction) by 26m long (y direction) and with wave absorbers

installed along all four lateral boundaries. In the present computer model, the basin domain dimensions are doubled in both directions in order to eliminate boundary effects for each configuration of islands considered. The still water depth h is 0.32m, and the Manning's roughness coefficient is 0.013 s/m$^{1/3}$. A circular island represented by a flat-topped cone is placed in the middle of the wave basin. The conical island has a based radius of 3.6m, a crest radius of 1.1m, and is of height 0.625m.

A grid size of $\Delta x = \Delta y = 0.05$ m is adopted for all test cases, corresponding to a grid of 1200 × 1040 square cells covering the flow domain. A time step of 0.01 s is selected, meeting the Courant-Friedrichs-Lewy condition. It should be noted that, in a separate study, Romer-Lee (2010) has examined the dependence of the computed results by the present model on grid resolution, and showed that the present grid size is sufficient to achieve converged solutions.

A solitary wave enters the domain from the boundary at $y = 0$ and propagates along the y axis. The flux normal to boundary is specified to be:

$$q = \left(1 + \frac{\eta}{h}\right) \cdot \eta \cdot \sqrt{gh} \qquad (19)$$

where

$$\eta = A \cdot \mathrm{sech}^2 \left[\sqrt{\frac{3A}{4h^3}} \cdot (2.2c - ct) \right] \qquad (20)$$

and the wave speed is $c = \sqrt{g(h + A)}$. This incident wave has amplitude A of 0.032 m, which is 10% of the still water depth. At the other three boundaries, a linear transmission boundary condition is applied whereby the normal derivatives of all the unknown quantities are specified to be zero. Although such a simple treatment does not strictly enforce a zero-transmission condition, the large computational domain ensures

that this is not a drawback, as the simulations have already stopped prior to the arrival of any unwanted disturbances generated as reflections at the boundaries.

Wetting/drying occurs around the island under the solitary wave attack. An empirical method of modelling this moving boundary problem is used, following Liang *et al.* (2007, 2010a). At each time step, drying and wetting checks are conducted. In the drying check, a computational node is regarded as dry if its water depth is less than 1 mm, and then excluded in the subsequent computation until switched wet again. It should be noted that the initial water levels are also assigned to the dry nodes, but they are equal to the ground levels to give a zero water depth. In the wetting check, the water level above a given dry node (called the frozen water level), is compared with the highest water level of any adjacent wet nodes (called the free water level). If the free surface level is found to be more than 2 mm higher than the frozen water level, then a 1 mm layer of water is shifted to the dry node from the corresponding wet node. The dry node may then be deemed wet and included in the subsequent computation. Numerical experiments have been conducted for the run-up around a single conical island and they reveal that the computational results are not sensitive to the threshold water depth adopted, which is consistent with ~~authors'~~Liang et al.'s (2007) experience o~~fn the~~ flood routing with the same wetting/drying technique ~~(Liang *et al.* 2007).~~

To improve the stability of the computation, a threshold still water depth, 5 mm, is prescribed, below which the dispersive terms are switched off and locally shallow water equations are solved. This treatment also removes the complications caused by the negative still water depths that are encountered in the numerical scheme during the run-up on island slopes.

4. Verification of the numerical model

Two validation cases are considered: (1) solitary wave propagation in otherwise still water over a flat bed; and (2) solitary wave run-up at a single conical island.

Figure 3 presents the free surface profiles for the solitary wave as it propagates forward over a horizontal bed at time t = 4, 9 and 14 s obtained from the present numerical model (a) with the dispersive terms switched off, and (b) including the Boussinesq terms. Figure 3(a) shows that a shallow-water modelled solitary wave has the tendency to shock-up into a steep, triangular shape over time, because the wave crest travels faster than the trough due to the finite change in water depth. No spurious oscillations arise from the almost vertical wave front, confirming the shock-capturing capability of the model. Conversely, Figure 3(b) shows that very little profile evolution occurs when the dispersive terms are included, demonstrating that the wave nonlinearity is countered by dispersion in the case of a solitary wave. The results are in satisfactory agreement with the analytical solution for a solitary wave of small amplitude, where the shape of the free surface profile remains nearly constant as the wave propagates. The results highlight the drawback of a shallow water model when applied to solitary wave propagation.

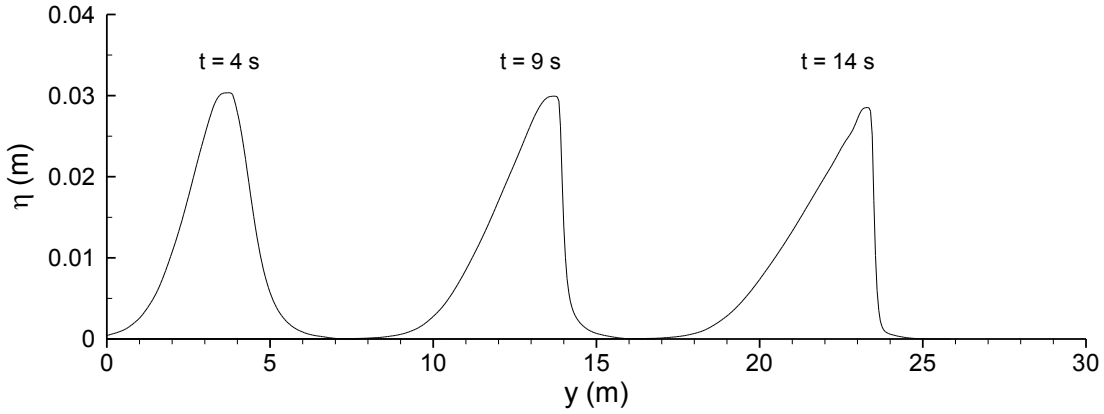

(a) without frequency dispersion (i.e. shallow flow equations)

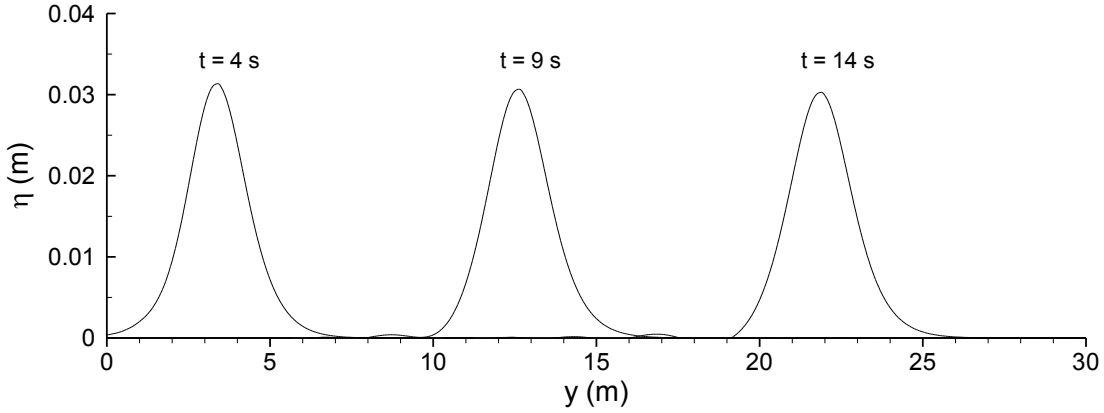

(b) with frequency dispersion (i.e. Boussinesq-type equations)

Fig. 3. Solitary wave propagation over a flat bed

The second validation test comprises solitary wave run-up at an isolated conical island, for which experimental measurements are available from the laboratory tests conducted by Liu *et al*. (1995). Figure 4 shows (a) the bed topography, positions of wave gauges, and (b), (c), and (d) colour visualisations of the free surface contours at times t = 16, 18 and 20 s respectively after the solitary wave was introduced into the domain. The vertical axis of Figure 4 has been magnified by a factor of two (relative to the horizontal axis) in order to improve the visualisation. The solitary wave slows down as it approaches the island, causing the wave front to curve near the shoreline. Figure 4(b) shows the situation as the island is struck by the solitary wave, with high run-up occurring at the front of the island. The solitary wave front that originally spanned across the entire domain is interrupted by the island and split into two waves (Figure 4(c)), each of which travel along the two sides of the island. Meanwhile, a reflected wave is created that begins to radiate out from the island (see Figure 4(c-d)). Later, the diffracted waves propagate alongshore and collide at the rear of the island (Figure 4(d)), generating a high run-up on the lee side, which is somewhat counterintuitive.

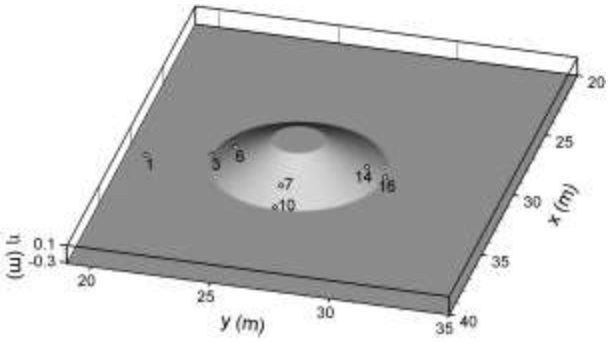

(a) Bed elevation and wave gauges

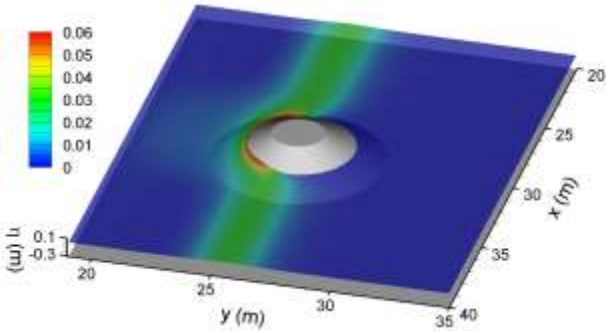

(b) t = 16 s

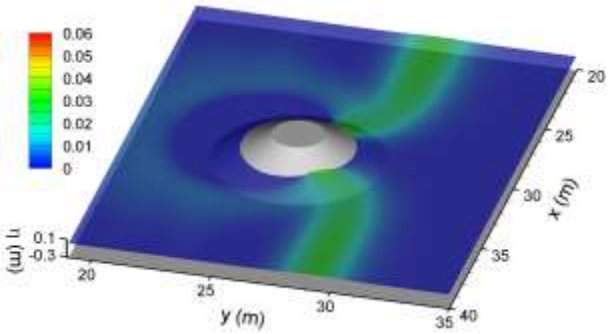

(c) t = 18 s

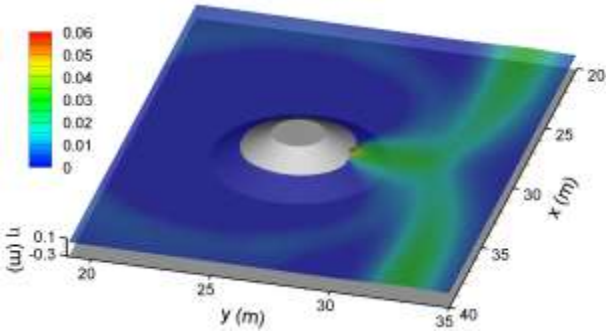

(d) t = 20 s

Fig. 4. Solitary wave interaction with a single conical island: bed topography and visualizations of predicted water surface elevations

Figure 5 plots the predicted and measured time histories of free surface elevations at several wave gauges, whose positions are labelled in Figure 4(a). In general, the model predictions match the experimental data, especially the amplitude of the main wave, until the solitary wave crest has passed. There are some discrepancies that become evident after the main wave has passed: the experimental profiles are more oscillatory, perhaps due to swash zone effects not being fully represented in the wetting and drying scheme, the effect being most obvious at Gauge 6. A more extensive comparison has been given by Romer-Lee (2010). However, it is evident that the numerical simulation satisfactorily reproduces the interactions between the solitary wave and the island.

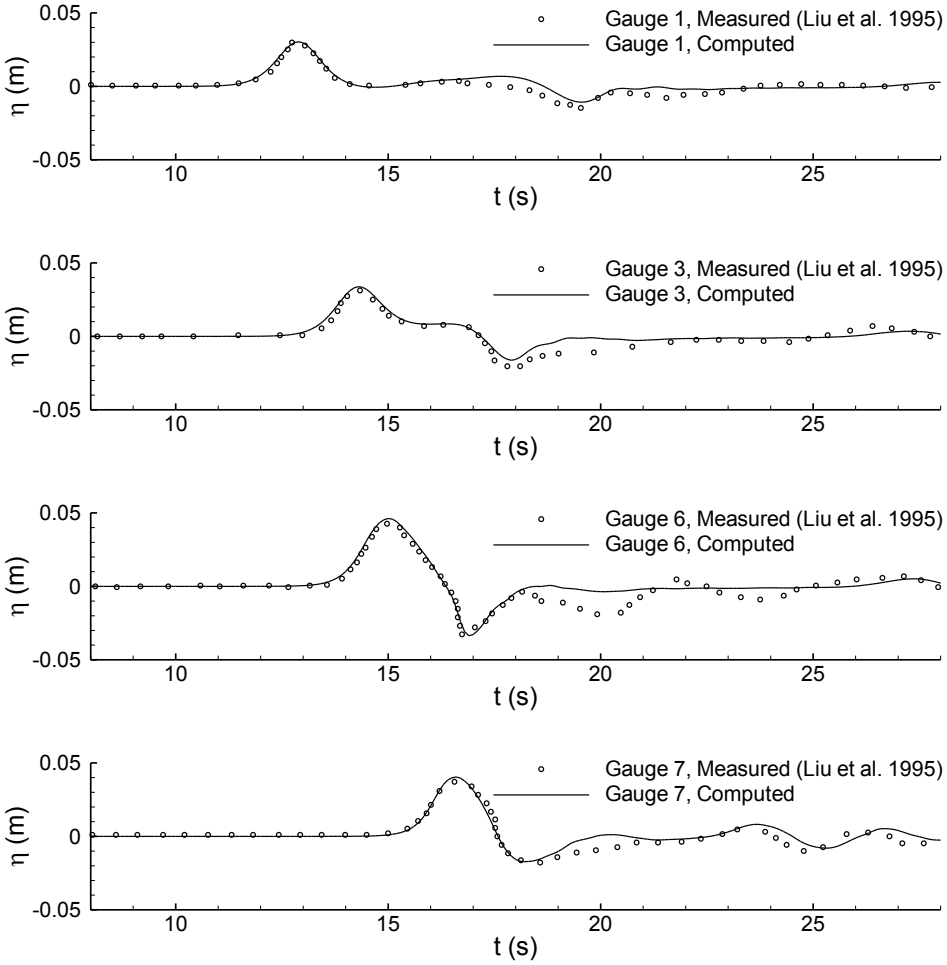

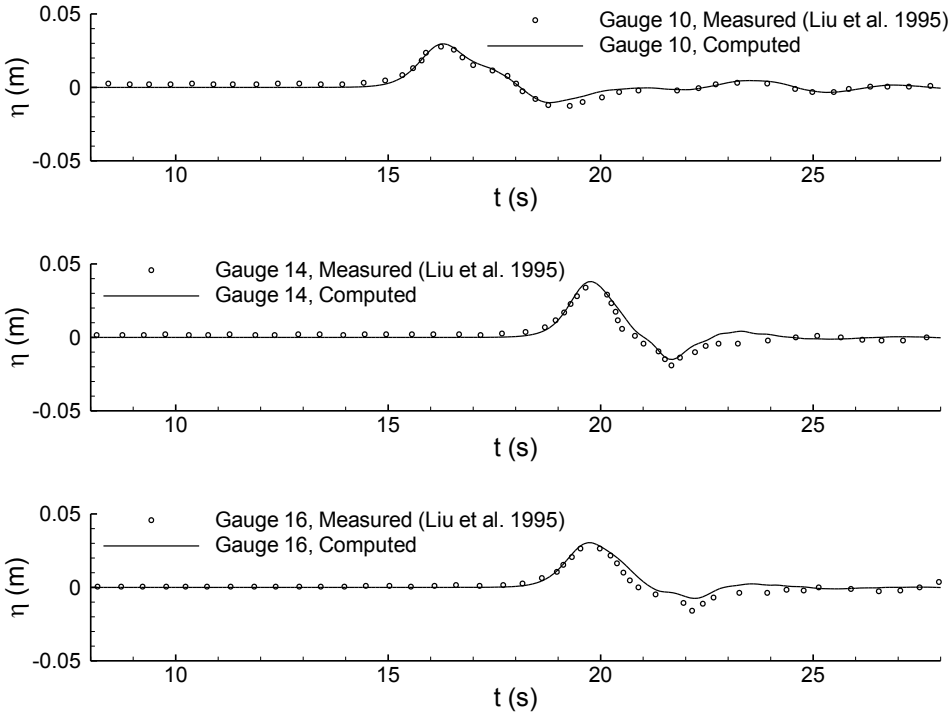

Fig. 5 Solitary wave interaction with a single conical island: measured (Liu *et al.* 1995) and predicted time series of free-surface displacements at wave gauges.

Wave run-up – the height above normal sea level that seawater reaches on land – is an important parameter by which to evaluate the destructive potential of a tsunami. Figure 6 displays the contour field of maximum water surface elevation obtained over the entire simulation. There are two regions of high run-up: a broad band at the front of the island directly facing the incoming wave; and a small region at the back of the island. Both regions experience run-up of similar magnitude. Also of note in Figure 6 is the wake induced by the presence of the island. The sheltered region with relatively small wave height occupies two wedges enclosed by angles between around 10^{o} and 30^{o} from the centreline of the basin.

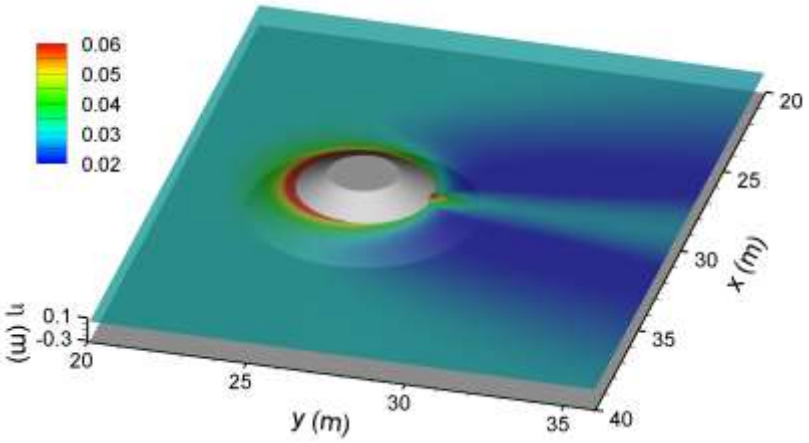

Fig. 6 Solitary wave interaction with a single conical island: colour contour visualization of predicted maximum water elevations

5. Solitary wave run-up on twin islands

Taking the above example of solitary wave interaction with a single conical island as a reference case, a second conical island is then added to the domain by altering the bed topography and initial water levels accordingly. All the other computational conditions are kept the same. To simplify the analysis, the two islands have the same shape and size. The definition sketch in Figure 7 shows the spacing and orientation of the islands relative to the incoming solitary wave in which d is the separation distance between the island centres and θ the relative angle. By varying these two parameters, the solitary wave run-up characteristics on the two islands are examined with respect to the island positions.

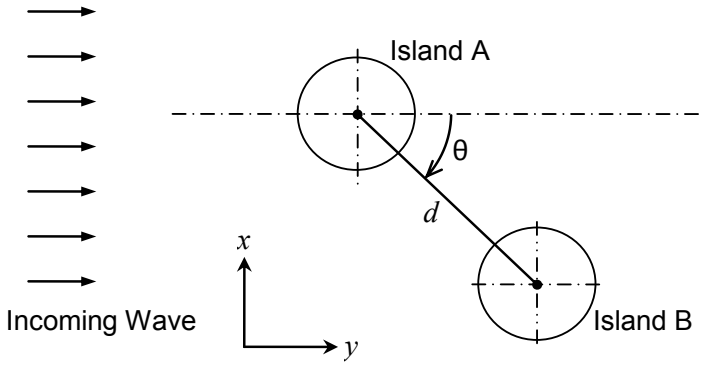

Fig. 7. Definition sketch of solitary wave interaction with a pair of conical islands: plan view of island locations and definition of symbols

As the destruction inflicted by a tsunami is closely related to the run-up height, the peak run-up is chosen here as the focal parameter in quantifying the severity of wave attack. The peak run-up $R_{\max}$ for each combination of d and θ is normalised against that for a single island $R_{\max 0}$, which has been found to be 0.0742 m (see Figure 6). The two islands overlap each other above still water level when d < 4.64 m, and so the analyses are split into two categories: (1) separate islands and (2) merged islands. This distinction is necessary, as the merged islands tend to have the same peak run-up on each of the two constituent islands. For separate islands, the results are presented for Island A (in Figure 7), and θ varied from 0^o to 180^o. For merged islands, A and B may be regarded as a single landmass, and so θ is varied between 0^o and 90^o. Simulations have been carried out with θ being varied in increments of 10^o for island separation distances d = 2.2, 2.7, 3.2, 3.7, 4.64, 5.5, 7.2, 10.8, 14.4, and 18.0 m. In the subsequent discussion, the distance is normalised by the island radius at still water level, R = 2.32 m.

Figure 8 shows the normalized solitary wave run-up $R_{\max}/R_{\max 0}$ as a function of relative angle θ and normalized separation distance d/R, obtained for the separate island simulations. Figure 9 presents visualisations of the maximum water surface levels $\eta_{\max}$

obtained for four configurations of island pairs. Using symmetry, the peak run-ups at two angles can be extracted from each plot in Figure 9, depending on how the islands are designated A and B. Figure 8 indicates that the presence of the Island B has almost no effect on R_{max} at Island A for $d/R > 3$ and $\theta < 120^{o}$. However, R_{max} reduces considerably as for $\theta \approx 150^{o} \sim 160^{o}$, recovering somewhat by $\theta = 180^{o}$, for $d/R > 4$. The trough at $\theta \approx 150^{o} \sim 160^{o}$ corresponds to cases where Island A is sheltered from the oncoming solitary wave by Island B (e.g. see Figure 9(a)). The wave amplitude recovers quickly behind a single island due to diffraction (see Figure 6), which explains why R_{max} increases at $\theta > 160^{o}$. For $d/R < 2.37$, the normalized maximum run-up $R_{max}/R_{max\,0}$ increases above unity when the two islands are in a tandem arrangement, i.e. $\theta \approx 0^{o}$ (or 180^{o}). This increase in maximum run-up when the two islands are in close proximity occurs because diffracted waves behind the front island collide with the reflected wave from the front face of the rear island. Figure 9(b) illustrates the situation when wave interaction in the narrow gap ($d = 2R$) between the two causes the water surface to reach elevations higher than at the head of the front island. Figure 9(c) shows that this phenomenon no longer occurs as d/R increases to 3.1. The trough in the run-up distribution in Figure 8 becomes shallower as d/R reduces. This is because the area sheltered by the front island is small in close vicinity. Figure 9(d) depicts the maximum water surface elevation obtained when the two islands are located side-by-side as they face the oncoming solitary wave front. For $d/R > 2$, the spacing between the islands is sufficient to permit a gap flow whenever the free surface elevation is greater than zero, preventing any enhancement of run-up at $\theta = 90^{o}$.

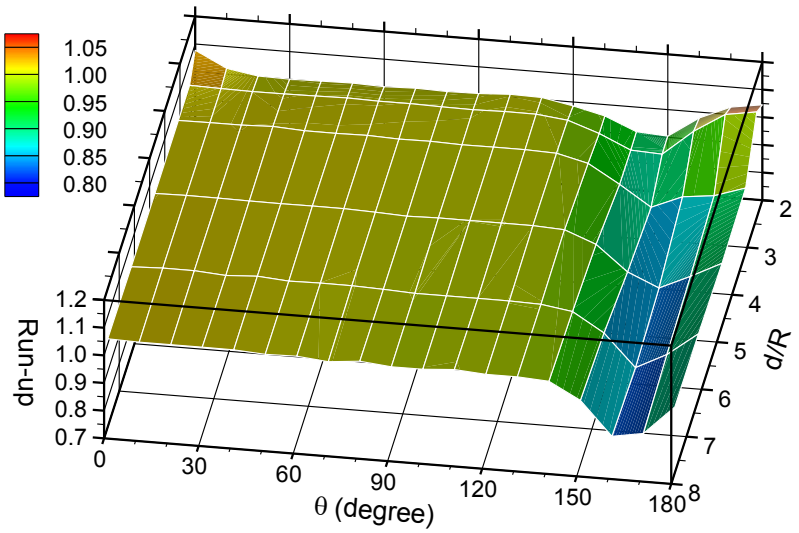

Fig. 8. Solitary wave interaction with separate pair of conical islands: normalised maximum run-up $R_{\max}/R_{\max 0}$ on island A as a function of relative angle θ and normalized separation distance d/R

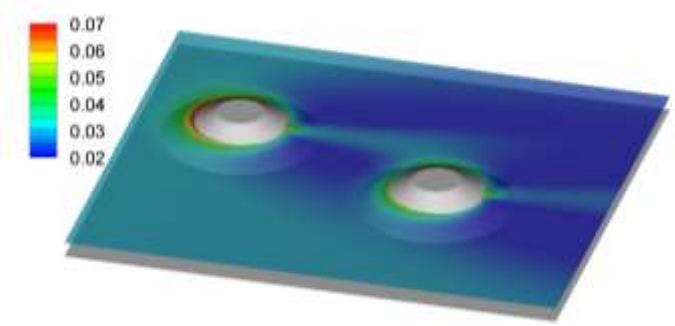

(a) $d = 4.66R$, $\theta = 20^{o}$ (160^{o})

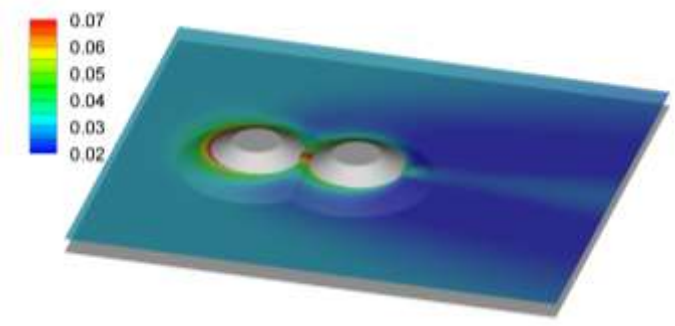

(b) $d = 2R$, $\theta = 0^o$ (180^o)

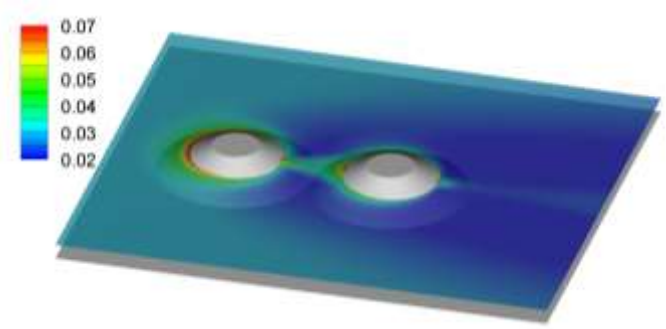

(c) $d = 3.10R$, $\theta = 0^o$ (180^o)

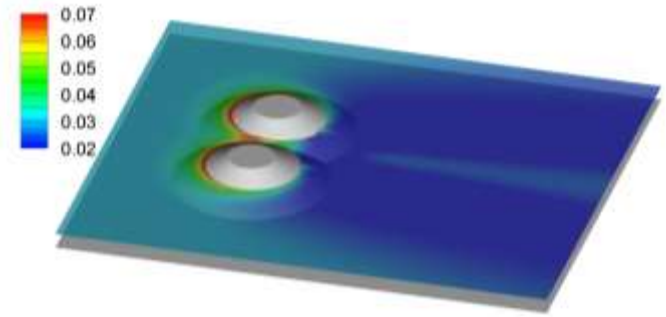

(d) $d = 2R$, $\theta = 90^o$

Figure 9. Solitary wave interaction with separate pair of conical islands: colour contour visualization of predicted maximum water elevations

It should be noted that the change in peak run-up $R_{max}/R_{max\,0}$ is only between -20% and +10% for the cases considered above of solitary wave interaction with separate conical islands. Figure 10 shows $R_{max}/R_{max\,0}$ as a function of θ and d/R for solitary wave interaction with merged conical islands. The value of $R_{max}/R_{max\,0}$ is always greater than unity, indicating that the merged conical islands consistently experience greater solitary wave run-up than the equivalent single conical island, within the range of parameters tested. Furthermore, the run-up height at the merged islands tends to increase monotonically with both d and θ. By comparing Figure 10 with Figure 8 it can

be seen that the value of $R_{max}/R_{max\,0}$ is consistently higher for the merged conical islands than for the separate conical islands, with the peak run-up for merged islands being amplified by as much as 50%, a significantly larger value than obtained for the separate conical islands. Figure 11 provides four representative plots of the maximum free surface elevation distribution for selected values of θ and d/R for the merged islands. It is evident that the highest free surface elevations (and hence run-up) tend to occur in the regions where the islands merge (i.e. between the island crests). This phenomenon is clearly seen in Figures 11(a) and 11(b) with $\theta = 90^o$ when the merged islands present the largest projected frontal area to the incoming solitary wave. Figures 11(c) and 11(d) show the maximum free surface elevation distributions obtained when the merged islands present the smallest projected frontal area, i.e. for $\theta = 90^o$. From the numerical results, the peak run-up at $d/R = 1.6$ occurs at the groove in the middle of the two islands (Figure 11(c)), whereas R_{max} occurs at the head of the front island when the two islands are spaced closer together at $d/R = 1.16$ (Figure 11(d)).

The above finding carries practical implications. Coastal development is often concentrated around narrow bay areas, where it appears sensible to construct urban settlements, ports, marinas, etc., presuming that such areas offer more protection from the wind and waves than exposed headlands. However, the above analyses show that narrow bay areas could be more prone to inundation from severe tsunami waves.

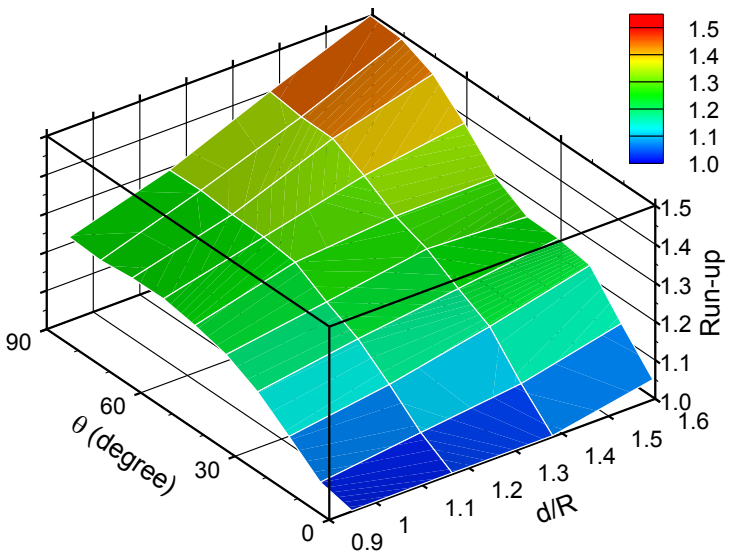

Fig. 10. Solitary wave interaction with merged pair of conical islands: normalised maximum run-up $R_{max}/R_{max\,0}$ as a function of relative angle θ and normalized separation distance d/R

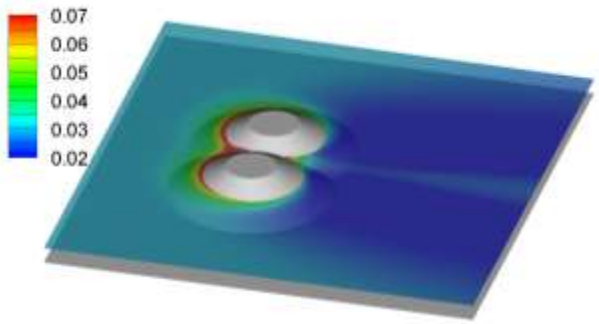

(a) $d = 1.60R$, $\theta = 90^{o}$

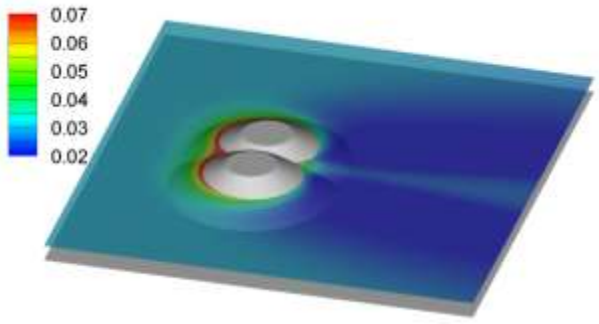

(b) $d = 1.16R$, $\theta = 90^{o}$

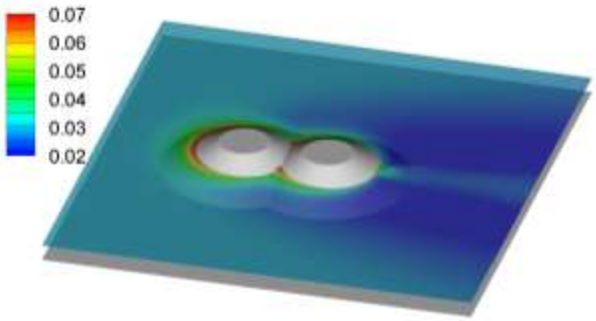

(c) $d = 1.60R$, $\theta = 0^{o}$

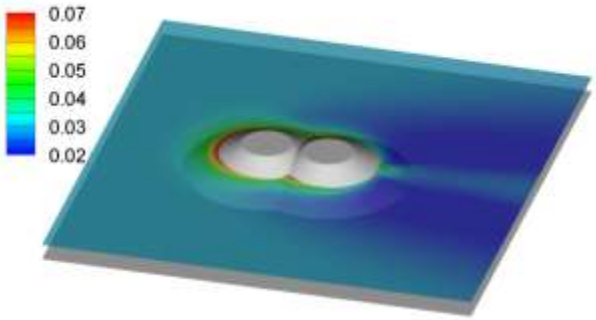

(d) $d = 1.16R$, $\theta = 0^{o}$

Fig. 11. Solitary wave interaction with merged pair of conical islands: colour contour visualization of predicted maximum water elevations

6. Conclusions

A shock-capturing TVD Lax-Wendroff numerical scheme has been applied to solve the Boussinesq-type equations of Madsen and Sørensen. Using operator-splitting, the two-dimensional problem has been converted into a pair of one-dimensional problems, each of which is solved efficiently using a tri-diagonal matrix algorithm. The model has been validated for the evolution of a solitary wave over a flat bed, emphasising the need to include the dispersive Boussinesq terms, and then verified for solitary wave run-up at a single conical island by comparison against experimental data obtained by Liu *et al.* (1995). The model is found to reproduce satisfactorily the main characteristics of the

wave behaviour. High values of run-up occur over much of the front face of the island. Due to the collision of diffracted waves behind the island, a narrow band of high values of run-up are also obtained at the back face of the island.

A parameter study was then undertaken whereby solitary wave interaction with a pair of identical conical islands was investigated for different spacing and relative angles, and the results presented as plots of non-dimensional maximum run-up and maximum free surface elevation. For relatively large $d/R \geq 3.1$, the maximum run-up occurs at the point on the island pair that is first impacted by the solitary wave. The maximum run-up does not exceed that of a single island because there is a sufficient time interval between the original solitary wave impact and the arrival of the reflected wave from the neighbouring island. For $\theta > 130^{o}$ with this large separation, the maximum run-up is less than that at a single island, because of the sheltering effect of the upstream island. For $2 \leq d/R \leq 2.37$, the two islands remain separate above still water level, and large free surface levels and run-up occur in the narrow gap region, influenced by wave-wave interactions, especially when the rear island is directly behind the front island. When the two islands merge into a single entity (even above high water level) with $d/R \leq 1.60$, the solitary wave is prevented from propagating between the island crests. The simulations have shown that the maximum run-up can be amplified by up to 150%, owing to the combined projected area of the front face of the island pair perpendicular to the solitary wave flow.

The present study has direct implications on assessing the tsunami risk to small volcanic islands. For closely spaced islands, the maximum free surface elevations and associated peak run-up due to a tsunami event may occur in the narrow bay region between the islands, close to where coastal development is often concentrated.

We are currently investigating the influence of the incident wave amplitude and the slope of the islandss' slope on the maximum run-up, and intend to report the findings in a future publicationthese results will be reported soon.

References

Borthwick A.G.L., Ford M., Weston B.P., Taylor P.H. and Stansby P.K. (2006). Solitary wave transformation, breaking and run-up at a beach. Journal of Maritime Engineering, 159: 97-105

Bradford S.F. and Sanders B.F. (2002). Finite volume schemes for the Boussinesq equations. Proceedings of the 4th International Symposium on Ocean Wave Measurement and Analysis – Waves 2001, San Francisco, USA.

Briggs M.J., Borrero J.C. and Synolakis C.E. (2005). Tsunami disaster mitigation research in the United States. International Symposium on Tsunami Mitigation in Future, Kobe, Japan, pp1-14

Briggs M.J., Synolakis C.E., Harkins G.S. and Green D.R. (1995). Laboratory experiments of tsunami runup on a circular island. Pure and Applied Geophysics. 144(3-4): 569-593

Chen Q., Kirby J.T., Dalrymple R.A., Kennedy A.B. and Chawla A. (2000). Boussinesq modelling of wave transformation, breaking, and runup. II: 2D. ASCE Journal of Waterway, Port, Coastal, and Ocean Engineering, 126(1): 48-56

Davis S.F. (1984). TVD finite difference schemes and artificial viscosity. ICASE Report No. 84-20. National Aeronautics and Space Administration, USA

Fuhrman D.R, Madsen P.A. (2008). Simulation of nonlinear wave run-up with a high-order Boussinesq model. Coastal Engineering, 55: 139-154

Godunov S.K. (1959). A difference scheme for numerical solution of discontinuous solution of hydrodynamic equations. Mathematics Sbornik, 47: 271-306

Jacaranda. (2002). Jacaranda atlas of the Pacific Islands. John Wiley and Sons Australia.

Liang D., Lin B. and Falconer R.A. (2007). Simulation of rapidly varying flow using an efficient TVD-MacCormack scheme. International Journal for Numerical Methods in Fluids. 53: 811-826.

Liang D., Wang X., Falconer R.A. and Bockelmann-Evans B.N. (2010a). Solving the depth-integrated solute transport equation with a TVD-MacCormack scheme. Environmental Modelling and Software, 25: 1619-1629

Liang D. (2010b). Eliminating discharge imbalances in predicting shallow water flows with shocks. Transactions of the Hong Kong Institution of Engineers (in press)

Liu P.L.-F., Cho Y., Briggs M.J., Kanoglu U. and Synolakis C.E. (1995). Runup of solitary waves on a circular island. Journal of Fluid Mechanics, 302: 259-285

Madsen P.A. and Sørensen O.R. (1992). A new form of the Boussinesq equations with improved linear dispersion characteristics. Part 2. A slowly-varying bathymetry. Coastal engineering, 18(3): 183-204

Lavigne F., Paris R., Grancher D., Wassmer P., Brunstein D., Vautier F., Leone F., Flohic F., De Coster B., Gunawan T., Gomez C., Setiawan A., Cahyadi R., and Fachrizal. (2009) Reconstruction of tsunami inland propagation on December 26, 2004 in Banda Aceh, Indonesia, through field investigations. Pure and Applied Geophysics, 166: 259-281

Minoura K., Imamura F., Takahashi T. and Shuto N. (1997) Sequence of sedimentation processes caused by the 1992 Flores tsunami: Evidence from Babi Island. Geology, 25(6):523-526.

Ning D.Z., Zang J., Liang Q., Taylor P.H. and Borthwick A.G.L. (2008). Boussinesq cut-cell model for non-linear wave interaction with coastal structures. International Journal for Numerical Methods in Fluids, 57: 1459-1483

Romer-Lee J.K. (2010). Modelling tsunami run-up on circular islands. MEng thesis, Univeristy of Cambridge.

Strang G. (1968). On the construction and comparison of finite difference schemes. SIAM Journal on Numerical Analysis, 5: 506-517.

Titov V.V. and Synolakis C.E. (1998). Numerical modelling of tidal wave runup. ASCE Journal of Waterway, Port, Coastal, and Ocean Engineering, 124(4): 157-171

Tsuji Y., Matsutomi H., Imamura F., Takeo M., Kawata Y., Matsuyama M., Takahashi T., Sunarjo and Harjadi P. (1995). Damage to coastal villages due to the 1992 Flores Island earthquake tsunami. Pure and Applied Geophysics, 144(3/4): 481-524

Wei Y., Mao X.Z. and Cheung K.F. (2006). Well-balanced finite-volume model for long-wave runup. ASCE Journal of Waterway, Port, Coastal, and Ocean Engineering, 132(2): 114-124

Yeh H., Liu P.L.-F., Briggs M., and Synolakis C.E. (1994) Tsunami catastrophe in Babi Island. Nature, 372: 6503-6508

Figures

Fig. 1. Computational procedure

Fig. 2. Computational stencil for two-step Lax-Wendroff scheme

Fig. 3. Solitary wave propagation over a flat bed

(a) without frequency dispersion (i.e. shallow flow equations)

(b) with frequency dispersion (i.e. Boussinesq-type equations)

Fig. 4. Solitary wave interaction with a single conical island: bed topography and visualizations of predicted water surface elevations

(a) Bed elevation and wave gauges

(b) $t = 16$ s

(c) $t = 18$ s

(d) $t = 20$ s

Fig. 5 Solitary wave interaction with a single conical island: measured (Liu *et al.* 1995) and predicted time series of free-surface displacements at wave gauges.

Fig. 6 Solitary wave interaction with a single conical island: colour contour visualization of predicted maximum water elevations

Fig. 7. Definition sketch of solitary wave interaction with a pair of conical islands: plan view of island locations and definition of symbols

Fig. 8. Solitary wave interaction with separate pair of conical islands: normalised maximum run-up $R_{\max}/R_{\max 0}$ on island A as a function of relative angle θ and normalized separation distance d/R

Figure 9. Solitary wave interaction with separate pair of conical islands: colour contour visualization of predicted maximum water elevations

(a) $d = 4.66R$, $\theta = 20^{\circ}$ (160°)

(b) $d = 2R$, $\theta = 0^{o}$ (180^{o})

(c) $d = 3.10R$, $\theta = 0^{o}$ (180^{o})

(d) $d = 2R$, $\theta = 90^{o}$

Fig. 10. Solitary wave interaction with merged pair of conical islands: normalised maximum run-up $R_{\max}/R_{\max 0}$ as a function of relative angle θ and normalized separation distance d/R

Fig. 11. Solitary wave interaction with merged pair of conical islands: colour contour visualization of predicted maximum water elevations

(a) $d = 1.60R$, $\theta = 90^{o}$

(b) $d = 1.16R$, $\theta = 90^{o}$

(c) $d = 1.60R$, $\theta = 0^{o}$

(d) $d = 1.16R$, $\theta = 0^{o}$